



Low-temperature NH₃-SCR of NO by lanthanum manganite perovskites: Effect of A-/B-site substitution and TiO₂/CeO₂ support

Runduo Zhang, Wei Yang, Na Luo, Peixin Li, Zhigang Lei, Biaohua Chen*

State Key Laboratory of Chemical Resource Engineering, Beijing University of Chemical Technology, Beijing, 100029, China

ARTICLE INFO

Article history:

Received 24 October 2012

Received in revised form 22 March 2013

Accepted 18 April 2013

Available online 26 April 2013

Keywords:

Mn-based perovskite

NH₃-SCR of NO

B-site substitution

CeO₂

TiO₂

ABSTRACT

A series of LaMn-based perovskites was fully characterized and tested for the selective catalytic reduction (SCR) of NO by NH₃ in the presence of O₂. The physicochemical properties, adsorbed species and surface reaction were investigated by means of N₂ sorption, XRD, XPS, H₂-TPR, NO + O₂- or NH₃-TPD, and in situ DRIFTS, in order to discriminate the effects of A- or B-site partial substitutions and their supports on SCR performances. With respect to the parent material, cation incorporation and support dispersion achieved the different enhancements in deNO_x activity, mainly due to their modifications in nitrites/nitrates and adNH₃ cumulants as well as redox capacity. For these prepared samples, an inhibition on the coverage of inert ionic nitrates was thought to be crucial to improve NO conversion at the high-temperature zone; while an increase in NO oxidation ability was considered to be important at temperatures below 200 °C, as observed over LaMnO₃/CeO₂. Besides, perovskite structure was apparently beneficial for this SCR process via largely enriching the surface manganese and oxygen species.

© 2013 Elsevier B.V. All rights reserved.

1. Introduction

Nitrogen oxides (NO_x), which may derive from the power plants, have been deemed to be a major source of air pollution in the modern society. Their continuous and abundant emission could lead to some serious environmental problems such as photochemical smog, acid rain, ozone depletion, and greenhouse effect [1,2]. Among all the methods for NO_x removal, selective catalytic reduction of NO_x by different reducing agents (NH₃, H₂ or hydrocarbons) has been regarded as a promising technology. H₂-SCR of NO_x has been widely studied since the beginning of this century [3–9], due to its excellent low-temperature activity with respect to NH₃ or HCs-SCR. Costa et al. [3–6], Savva and co-workers [6,7] and Olympiou et al. [8] reported interesting results on this reaction, focusing on MgO-CeO₂ or perovskite supported Pt catalysts. NH₃-SCR is also considered to be one of the most efficient and economic technologies [1,2,10]. Nowadays, the commercial catalyst for this process is V₂O₅-WO₃(MoO₃)/TiO₂, which shows a satisfactory deNO_x performance and stability under 300–400 °C [11]. However, in order to avoid the catalyst deactivation caused by the poisoning of high concentrations of ash and SO₂, SCR unit is suggested to be located at the downstream of the electrostatic precipitator and desulfurizer [1]. Consequently, the temperatures of flue gas are commonly around 200 °C or even lower [12]. To avoid reheating, the development of the low-temperature SCR catalysts has attracted lots

of attention in the academic community. Many transition metal-based catalysts was accordingly investigated for low-temperature SCR of NO by NH₃, such as MnO_x/Al₂O₃ [13], V₂O₅/activated carbon [14], Fe_xMn_{1-x}TiO_y [10]. Thereamong, the supported manganese oxides have attracted substantial attention, due to their excellent low-temperature activities in this reaction [2,10,11].

Perovskites are the mixed oxides having ABO₃ general formula. Some of the possible compositions (with a lanthanide in the A-position and a transition metal in the B-position) are proved to be effective environmental catalysts for SCR of NO_x by diverse reductants, such as C₃H₆ [15–18] and CO [19], as well as the total oxidation of CO [20], CH₄ [21], VOCs [22,23], etc., due to their excellent high-temperature thermal and hydrothermal stabilities, great versatility, flexible compositions, and excellent redox properties, in addition to a limited cost of the constituting elements. However, the study of low-temperature NH₃-SCR of NO over perovskites is scarce in the literature even though Mnⁿ⁺, which is highly dispersed in the B sites of LaMn-based perovskites, might have a comparable activity and better stability than that in MnO_x. In order to further improve the catalytic properties of perovskites, A- or B-site substitution as well as a successive dispersion by diverse supports has been considered. [15,24,25]. Among the wide variety of non-noble metal cations that can be partially incorporated into the perovskite structure, Ce and Sr (in A-site) as well as Fe and Cu (in B-site) have been proved to be very effective to improve the catalytic performances for VOCs combustion [21,23]. However, Cu-containing catalysts may not be suitable for the application in the present NH₃-SCR of NO reaction because Cu was reported to be an outstanding NH₃ slip (oxidize NH₃ by O₂) catalyst rather than a NH₃-SCR one

* Corresponding author. Tel.: +86 10 64412054; fax: +86 10 64436787.

E-mail address: chenbh@mail.buct.edu.cn (B. Chen).

[26]. Moreover, vanadium substitution is likely beneficial for NO elimination since it has displayed the good activity as a successfully commercial SCR catalyst. Besides, the supporting of perovskites by TiO₂ and CeO₂ were deemed to be helpful for NH₃-SCR of NO [2,11].

In this manuscript, NH₃-SCR of NO was systematically studied over Mn-based perovskites, using N₂-sorption, XRD, XPS, H₂-TPR, NO + O₂-TPD, NH₃-TPD, and *in situ* DRIFTS, aiming at clarifying the effect of modifications (including A- or B-site substitutions and dispersion by support) on the related catalytic performances, revealing the principle to design a highly active perovskite-type catalyst for this low-temperature SCR process.

2. Experimental

2.1. Materials

LaMnO₃, La_{0.9}A_{0.1}MnO₃ (A = Sr, Ce) and LaMn_{0.95}B_{0.05}O₃ (B = Fe, V) perovskites were synthesized according to the classical citrate complexation procedure [27,28]. Stoichiometric amounts of the metallic nitrates were firstly dissolved into the distilled water. Thereafter, an aqueous solution of citric acid (CA), containing a number of mol of CA equal to those of the equivalent cations, was slowly added to the precursor solution under gentle stirring. Solvent evaporation was performed at 80 °C until the formation of a gel. Afterwards the gel was dried in an oven at 110 °C during 24 h. Subsequently, the foam solid was crushed and calcined at 600 °C for 3 h (ramp rate = 5 °C min⁻¹). Additionally, the foam precursor of LaMnO₃ was also calcined at 500 °C for 3 h, obtaining a sample denoted as La—Mn—O. La₂O₃ and Mn₂O₃ were mixed and fully ground, following a thermal treatment of 600 °C for 3 h (denoted as La₂O₃—Mn₂O₃).

LaMnO₃/MO₂ (M = Ti, Ce) catalysts were prepared in accordance with the literature [29], both with a mass ratio of 2:5 (LaMnO₃:MO₂). Initially, CeO₂ and TiO₂ supports were synthesized in the different ways. In the case of TiO₂, the preparation was carried out through a sol–gel method, using tetrabutyl titanate (C₁₆H₃₆O₄Ti) as the precursor. 0.1 mol of C₁₆H₃₆O₄Ti and 0.4 mol of C₂H₅OH were mixed as solution A. 0.3 mol of CH₃COOH, 0.4 mol of C₂H₅OH as well as 0.4 mol of the deionized water were also mixed sufficiently as solution B. Afterwards, the solution B was slowly added to the solution A under stirring, and this mixture was kept stirring at room temperature for 24 h then dried at 80 °C for another 24 h, followed by calcination at 500 °C for 3 h. CeO₂ was obtained simply by calcining the precursor Ce(NO₃)₃ in air at 500 °C for 3 h. Thereafter, to prepare LaMnO₃/MO₂, only one modification is conducted in a typical synthesis of LaMnO₃ described above: the prepared support was added into the mixed solutions, which contain La, Mn nitrates and citric acid, under a stirring.

2.2. Characterization

X-ray diffraction (XRD) was carried out using X-ray diffractometer equipped with a Cu K α radiation ($\lambda = 0.15406$ nm) (D8FOCUS, Bruker). Diffractograms were collected in the 2θ range between 20° and 80° by step of 0.05° (step time = 5 s). Phase identification was made by comparison with JCPDS database while the crystallite sizes were calculated on the basis of Scherrer equation after Warren's correction for the instrumental broadening.

A Sorptomatic 1990 instrument (Thermo Electron) was used to measure the specific surface area (S_{BET}) of the samples at liquid N₂ temperature (-196 °C), using the Brunauer–Emmett–Teller (BET) method, with outgas pretreatment at 200 °C under vacuum.

X-ray photoelectron spectroscopy (XPS) was conducted on a Thermo-Fisher ESCALAB 250 system with Al K α radiation under

ultrahigh vacuum (UHV). The binding energy (BE) was calibrated with respect to the C 1s value of a contaminated carbon at 285.0 eV.

Prior to H₂-TPR experiment, each material (50 mg) was pre-treated at 600 °C under 20% O₂ in He in a flow rate of 20 mL min⁻¹ for 30 min. After cooling down to 30 °C, a He flow containing 5% H₂ with a flow rate of 20 mL min⁻¹ was initially stabilized, and then the temperature of the reactor increased from 30 °C to 800 °C with a ramp of 5 °C min⁻¹. Evolution of the H₂ concentration along with temperature was on-line recorded by TCD, and a water trap filled with a mixture of dry ice and ethanol was used before the TCD. The quantification of H₂ consumed was performed after the calibration of TCD.

NO + O₂-, NH₃-temperature programmed desorption (NO + O₂-TPD, NH₃-TPD) experiments were performed using a home-made temperature programmed characterization system equipped with a fixed-bed continuous-flow reactor and a quadrupolar mass spectrometer (OmniStar, MS200). 50 mg of each sample was pre-treated respectively by 1000 ppm NO + 6% O₂ (for NO + O₂-TPD) or 1000 ppm NH₃ (for NH₃-TPD) at 200 °C for 1 h, balanced by Ar (total flow rate = 20 mL min⁻¹). Subsequently, reactor was cooled down to 30 °C under the same atmosphere and purged with 20 mL min⁻¹ of Ar for 1 h to remove all weakly adsorbed molecules. Thereafter, the pretreated samples were flushed with 20 mL min⁻¹ of Ar, and temperature increased up to 500 °C with a ramp of 5 °C min⁻¹. The O₂, NO, N₂O, NO₂ and N₂ desorbed during NO + O₂-TPD experiments were simultaneously detected and recorded by MS with mass numbers of 32, 30, 44, 46 and 28, respectively. The cracking of NO₂ to NO was also considered in estimating the net signal of NO. Moreover, NH₃ desorbed during NH₃-TPD was monitored with the mass number of 16.

In situ diffuse reflectance infrared Fourier transform spectroscopy (DRIFTS) was conducted with an infrared spectrometer (TENSOR 27, BRUKER), which was equipped with a high sensitive MCT detector and a diffuse reflection accessory including a high-temperature reaction chamber (Praying Mantis, Harrick). The temperature of the reaction chamber was controlled by an automatic temperature controller (Harrick). The reaction chamber was charged with the tested sample, the temperature of which was then raised to 200 °C under He (20 mL min⁻¹). When the infrared signal was stabilized, the feeding gases were introduced into the chamber. IR spectra were recorded by accumulating 64 scans at a spectrum resolution of 4 cm⁻¹.

2.3. Catalytic activity measurement

SCR of NO by NH₃ was performed in a tubular microreactor. 200 mg (grain size = 250–425 μm) of material was inserted into the reactor under an atmosphere of 1000 ppm NO, 1000 ppm NH₃, 6% O₂ and balanced by Ar with a total flow rate of 100 mL min⁻¹ (corresponding to a GHSV of 30,000 h⁻¹). The temperature was increased from 100 to 400 °C in 50 °C intervals. The effluent gases composition (NO, NH₃, N₂O and NO₂) was analyzed using a multigas FT-IR spectrophotometer (NEXUS 470, Nicolet) fitted with an ultra-mini long path gas cell (Model 2.4-H, Infrared Analysis). N₂ concentration was determined using a gas chromatograph (GC, HP5890) equipped with TCD for quantification and combined columns of 5A and TDX-01 for separation.

3. Results and discussion

3.1. Physicochemical properties

As seen from Fig. 1 presenting X-ray diffraction patterns of all the samples, a pure perovskite-type structure was achieved for LaMnO₃ prepared through a thermal treatment at 600 °C, attributed to a

Table 1

Physical and structural properties of LaMn-based samples.

Sample	Crystalline phases ^a	S_{BET} ($\text{m}^2 \text{g}^{-1}$)	D (nm) ^b
La—Mn—O	Amorphous; weak La_2O_3 , P	41.6	
LaMnO_3	P	36.5	14.4
$\text{La}_2\text{O}_3\text{—Mn}_2\text{O}_3$	La_2O_3 , Mn_2O_3 ; minor Mn_3O_4	28.2	20.9 (La_2O_3)
$\text{La}_{0.9}\text{Ce}_{0.1}\text{MnO}_3$	P	31.1	15.0
$\text{La}_{0.9}\text{Sr}_{0.1}\text{MnO}_3$	P	32.6	16.3
$\text{LaMn}_{0.95}\text{Fe}_{0.05}\text{O}_3$	P	31.9	13.7
$\text{LaMn}_{0.95}\text{V}_{0.05}\text{O}_3$	P	37.8	12.5
$\text{LaMnO}_3/\text{CeO}_2$	CeO_2 ; minor P	58.2	4.40 (CeO_2)
$\text{LaMnO}_3/\text{TiO}_2$	TiO_2 ; minor P	64.2	8.60 (TiO_2)

^a Crystalline phases detected by XRD (P, perovskite).^b Crystal domain size calculated using the Scherrer equation $D = K\lambda/(\beta \cos \theta)$ after Warren's correction for instrumental broadening ($\beta^2 = B^2 - b^2$, where B is the FWHM and b is the instrumental broadening determined by the FWHM of the X-ray reflexion of SiO_2 , having particles larger than 150 nm, at $2\theta \approx 27^\circ$).

$\text{LaMnO}_{3.15}$ orthorhombic symmetry with $Pnma$ space group (JCPDS File no. 89-2470). It is noted that, stoichiometric LaMnO_3 , with a distorted orthorhombic perovskite structure as a consequence of Jahn-Teller distortion of the oxide octahedron around Mn^{3+} ion, could merely be prepared under a reducing or inert atmosphere, as announced by Elemans et al. [30]. In air, the overstoichiometric $\text{LaMnO}_{3+\delta}$ with oxygen excess would be synthesized accompanied by the formation of Mn^{4+} ions in order to reduce the static Jahn-Teller distortion of Mn^{3+} , leading to a mixed valence state of $\text{Mn}^{4+}/\text{Mn}^{3+}$ in the structure.

As the calcination temperature dropped to 500 °C, a mainly amorphous phase was obtained for La—Mn—O sample along with the weak signals of La_2O_3 (no. 74-1144) and $\text{LaMnO}_{3.15}$. Only diffractions of La_2O_3 , Mn_2O_3 (no. 89-4836) and minor Mn_3O_4 (no. 89-4837) could be detected after calcining the $\text{La}_2\text{O}_3\text{—Mn}_2\text{O}_3$ mixture at 600 °C, in good agreement with the literature [31,32] that perovskite preparation through a traditionally ceramic method usually involves a temperature as high as 800 °C to ensure the formation of the crystalline phase. A- or B-site partial substitutions did not introduce any other impurity phases, indicating that these metallic cations readily incorporate into the LaMnO_3 lattice (Fig. 1). Nevertheless, the formation of tiny external metal oxides, invisible

by XRD, cannot be totally excluded. No shift of the reflection peaks was observed after substitutions. Being supported on CeO_2 or TiO_2 , the diffraction peaks related to $\text{LaMnO}_{3.15}$ nearly vanished. This is mostly due to the dilution of perovskite phase by the supports. High dispersion of LaMnO_3 on these supports resulting in its small crystal size might be another explanation for this phenomenon.

As gathered in Table 1, the crystal sizes (D) of the pure perovskites are found to vary from 12.5 nm ($\text{LaMn}_{0.95}\text{V}_{0.05}\text{O}_3$) to 16.3 nm ($\text{La}_{0.9}\text{Sr}_{0.1}\text{MnO}_3$), while the specific surface areas (S_{BET}) change from $31.1 \text{ m}^2 \text{ g}^{-1}$ ($\text{La}_{0.9}\text{Ce}_{0.1}\text{MnO}_3$) to $37.8 \text{ m}^2 \text{ g}^{-1}$ ($\text{LaMn}_{0.95}\text{V}_{0.05}\text{O}_3$). It is known that, in comparison with LaMnO_3 , no obvious modification in D and S_{BET} was observed by these A- or B-site substitutions. Additionally, the formation of perovskite structure led to a slight diminution of the surface area (LaMnO_3 vs. La—Mn—O), which is correlated to a thermal treating at relatively higher temperature (600 °C vs. 500 °C). Moreover, the lowest surface area was obtained in the case of $\text{La}_2\text{O}_3\text{—Mn}_2\text{O}_3$. The large improvement in S_{BET} by CeO_2 or TiO_2 likely corresponds to both the high specific surface areas of the supports and the high dispersion of LaMnO_3 over them.

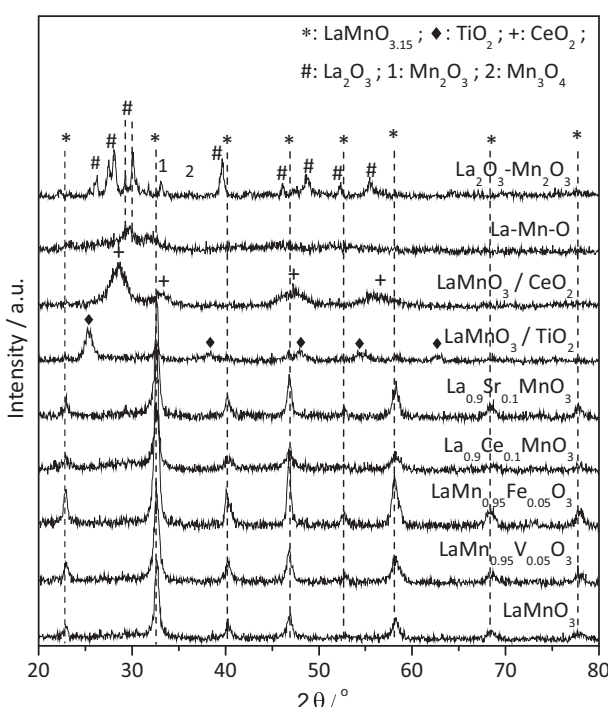
3.2. Influence of the crystal structures of perovskite

In order to reveal the role of perovskite crystal structure on SCR of NO by NH_3 , activity test was conducted among three La- and Mn-containing samples: perovskite (LaMnO_3), amorphous precursor (La—Mn—O) and mixture of the corresponding simple oxides ($\text{La}_2\text{O}_3\text{—Mn}_2\text{O}_3$). As illustrated in Fig. 2, similar parabolic curves of NO conversion were seen for the tested samples, with an activity order of $\text{LaMnO}_3 \gg \text{La}_2\text{O}_3\text{—Mn}_2\text{O}_3 > \text{La—Mn—O}$. Thereamong, LaMnO_3 achieved the best performance with NO conversions higher than 70% at 200–300 °C, showing a great contribution of the perovskite crystal structure on SCR performance.

For a further investigation, the surface element concentrations and valence states of these three solids were characterized by XPS. The results are reported in Fig. 3 and Table 2. As depicted in Fig. 3A, LaMnO_3 exhibited the highest surface Mn^{n+} concentration; while the weakest one was obtained on the surface of $\text{La}_2\text{O}_3\text{—Mn}_2\text{O}_3$, which is in keeping with the different values of La/Mn ratio (1.3 for $\text{LaMnO}_3 < 1.93$ for La—Mn—O $\ll 9.17$ for $\text{La}_2\text{O}_3\text{—Mn}_2\text{O}_3$, in Table 2).

Table 2XPS results for LaMnO_3 , La—Mn—O and $\text{La}_2\text{O}_3\text{—Mn}_2\text{O}_3$.

Samples	Surface abundance from XPS				
	La/Mn	$\text{O}_{\text{lattice}}^{\text{a}}$	$\text{O}_{\text{adsorbed}}^{\text{a}}$	$\text{O}_{\text{OH}^-}^{\text{a}}$	Total O ^a
LaMnO_3	1.30	1.00	1.20	0.85	3.05
La—Mn—O	1.93	0.25	0.32	0.13	0.70
$\text{La}_2\text{O}_3\text{—Mn}_2\text{O}_3$	9.17	0.19	0.67	0.18	1.04

^a Relative surface abundance of each oxygen specie is calculated by deconvolution of O 1s XPS peaks. The peak area of lattice oxygen on LaMnO_3 is denoted to be 1.00.**Fig. 1.** XRD patterns for LaMn-based samples.

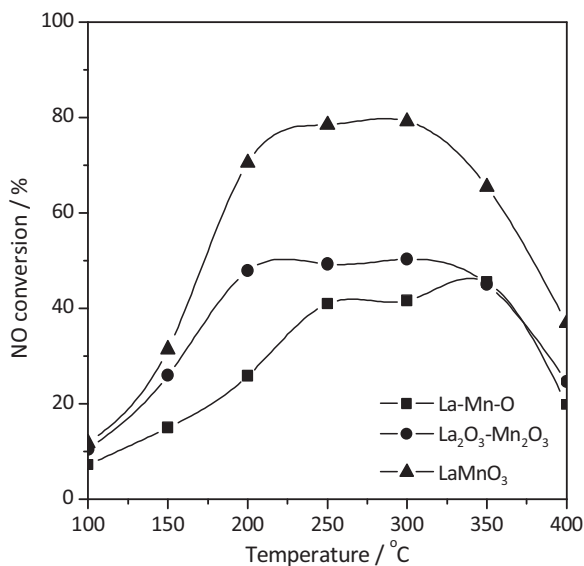


Fig. 2. NO conversion in NH₃-SCR of NO over LaMnO₃, La—Mn—O and La₂O₃—Mn₂O₃.

Such a result gives a clue that the distinct Mn contents could be correlated to the diverse crystal structures: perovskite structure is in favor of a better dispersion of Mnⁿ⁺ by its B-sites in the lattice resulting in a higher surface contents, as evidenced by XPS, than that of the amorphous (La—Mn—O) or mixture one (La₂O₃—Mn₂O₃). Nevertheless, the surface atom ratio of La/Mn for the present LaMnO₃ (1.3) is much larger than that obtained from the mesoporous La—Mn—O (0.15) reported in the early study [33], suggesting that perovskite structure is also beneficial for the surface enrichment of La. Additionally, the bands appearing in the range of about 640–645 eV and 650–660 eV are assigned to Mn 2p_{3/2} and 2p_{1/2} levels, respectively. Unfortunately, it is impossible to exactly distinguish and quantify the corresponding peaks for Mn²⁺ (640.9 eV), Mn³⁺ (641.8 eV) and Mn⁴⁺ (642.5 eV) in the Mn 2p_{3/2} region, but Mn²⁺ can be easily identified by its satellite peak at 648.8 eV [34–37]. Therefore, it seems that Mn²⁺ never existed on the surface of these samples. This also confirmed that in LaMnO₃ perovskite

structure, Mnⁿ⁺ existed in a mixed valence states of Mn⁴⁺/Mn³⁺, due to the Jahn-Teller distortion, which has been reported to be highly active in SCR process [16]. As for the surface oxygen species (Fig. 3B and Table 2), the formation of perovskite structure again achieved the highest surface oxygen contents [total oxygen, 2.73 (LaMnO₃) vs. 0.70 (La—Mn—O) or 1.04 (La₂O₃—Mn₂O₃), Table 2]. As mentioned in the literature, the bands at 529.2 eV, 531.2 eV and 532.9 eV can be individually assigned to lattice oxygen, surface adsorbed oxygen and oxygen in surface hydroxyl group [38]. Apparently, more lattice oxygen can be detected on the surface of LaMnO₃ with respect to La—Mn—O and La₂O₃—Mn₂O₃ (1.00 vs. 0.25 and 0.19), corresponding to the feature of perovskite structure. However, the last one (La₂O₃—Mn₂O₃) shows better oxygen adsorption ability than the amorphous La—Mn—O precursor (0.67 vs. 0.32). Surface chemisorbed oxygen has been reported to be extremely active in oxidation reaction due to its higher mobility than lattice oxygen [10]. Herein, the lower NO conversion achieved over La—Mn—O with respect to La₂O₃—Mn₂O₃ could be partially attributed to the lack of chemisorbed oxygen for NO oxidation, which deems as a necessary step for the SCR process, especially at low temperatures [39]. More importantly, as the active site, the surface concentration of Mnⁿ⁺ is essentially crucial for a satisfactory activity, whatever the reaction is. Based on the results above, it is concluded that, perovskite structure brings a remarkable improvement on NO conversion by enriching Mnⁿ⁺ and oxygen species (especially adsorbed oxygen) on the surface.

3.3. Effects of A- or B-site substitution and supporting

3.3.1. Activity tests

Fig. 4 shows the temperature dependence of NO and NH₃ conversions as well as N₂ yield for SCR of NO by NH₃ at 6% O₂ over the substituted and supported LaMnO₃ samples. As presenting in Fig. 4A–C, the modifications (including A- or B-site substitution and CeO₂ or TiO₂ supporting) of LaMnO₃ did not allow to change the total tendency that NO conversion decreased gradually above 300 °C. Such a decline can be partially assigned to the rapid consumption of NH₃ reductant through an unselective O₂ oxidation rather than SCR at the relatively higher temperatures. There was thus an obvious competition between NO and O₂ for the reaction with NH₃, i.e. between SCR and direct oxidation [15,18]. The oxidation of NH₃ could possibly contribute to the abundant existence of NO at high temperatures. In order to identify the contribution of NH₃ oxidation to the real NO conversion, the activity test for NH₃ oxidation is conducted over LaMnO₃ (not shown). It was observed that NH₃ could be intensely oxidized by O₂ above 200 °C with N₂O as the main product. As a byproduct, NO kept really low yield (within 5% below 400 °C) and its contribution to the decline of NO conversion in Fig. 4 was therefore minor. In fact, the oxidation of NH₃ towards NO by O₂ in SCR process is believed to be difficult since abundant NO has already existed in the exhaust, and the possibly formed NO was verified to react with the adsorbed NH₃ species readily to produce N₂O (or even N₂) according to a transient isotopic study on NH₃ oxidation [40]. Thus, it seems to be practicable to ignore this contribution over LaMn-based perovskites. Additionally, the possible generation of inert ionic nitrate species over LaFe_{1-x}(Cu,Pd)_xO₃ perovskites at high temperature, which can firmly occupy the active sites, might have a negative effect on NO conversion. Such species has been pointed out in our previous study [18]. Taking the N₂ yield into consideration, it was always close to NO and NH₃ conversions at 100 and 150 °C over all the samples, implying that the SCR reaction was dominant at low temperatures. Arriving at 200 °C, NO conversions stepped into their highest conversion platforms, and widened the gap along with

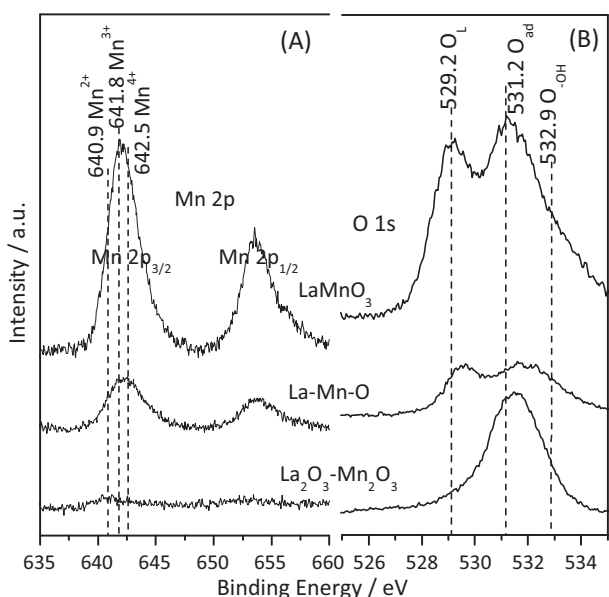


Fig. 3. XPS profiles for LaMnO₃, La—Mn—O and La₂O₃—Mn₂O₃. (A) Mn 2p, (B) O 1s.

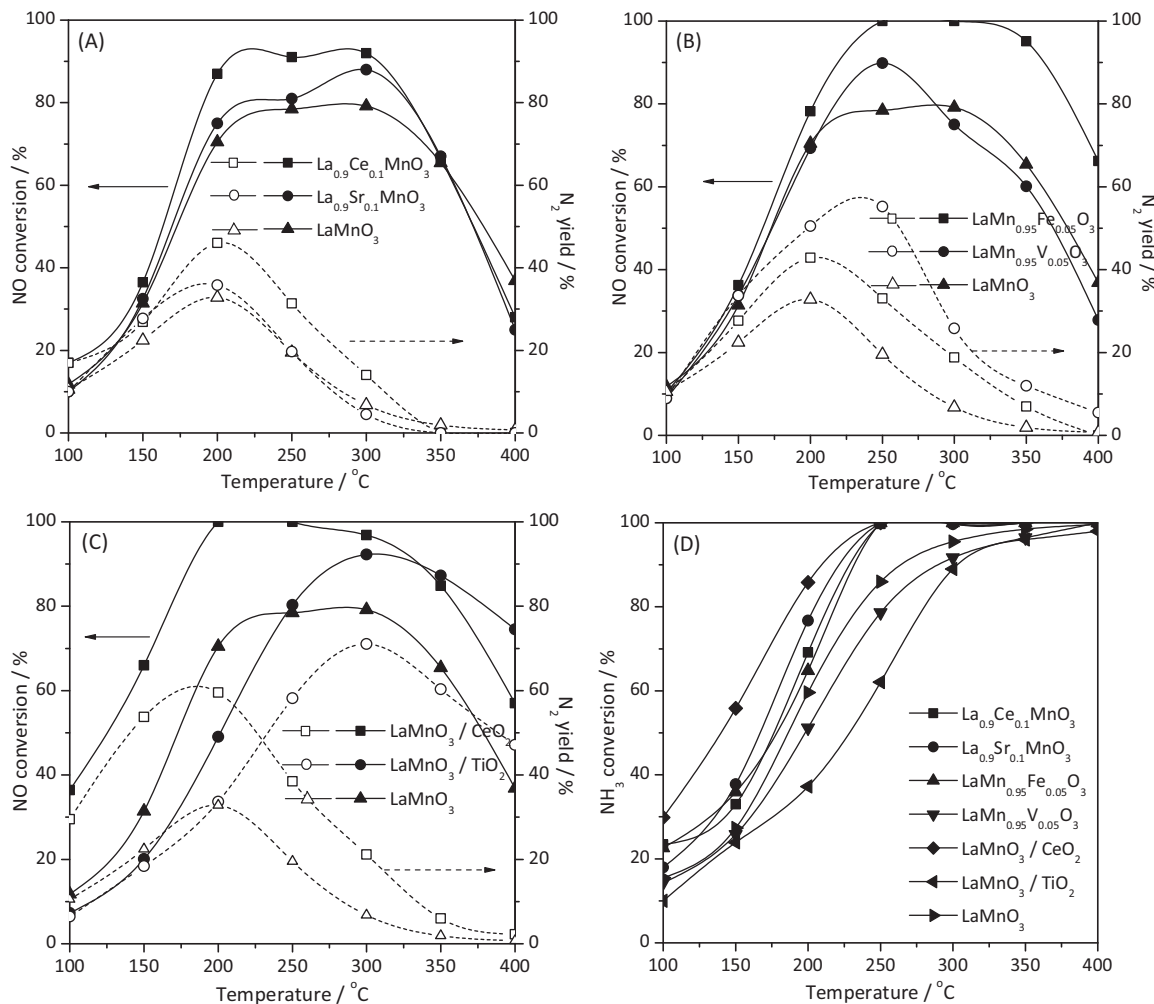


Fig. 4. Catalytic performances for the SCR of NO by NH₃ over LaMn-based samples: NO conversions over LaMnO₃ and (A) La_{0.9}A_{0.1}MnO₃ (A = Ce, Sr), (B) LaMn_{0.95}B_{0.05}O₃ (B = Fe, V), (C) LaMnO₃/MO₂ (M = Ce, Ti); (D) NH₃ conversions over all the samples. Conditions: GHSV = 30,000 h⁻¹, 1000 ppm NO, 1000 ppm NH₃, 6% O₂.

their corresponding N₂ yields. Simultaneously, NO₂ and N₂O were generated (no shown), confirming the occurring of unselective oxidation of NO and NH₃. However, it is impossible to distinguish the sources of these NO_x byproducts, since NO₂ could be produced by either NO or NH₃ direct oxidation, and N₂O might be generated from NO dissociation or NH₃ oxidation. By partial substitution of La³⁺ in A-sites, Ce⁴⁺ induced the considerable enhancements in NO and NH₃ conversions as well as N₂ yield; whereas, the limited improvement was obtained by Sr²⁺ incorporation (Fig. 4A). In the case of B-site substitutions, a complete NO conversion and an increasing N₂ yield were observed over Fe-containing sample. An excellent N₂ yield up to 60% was seen at 250 °C for LaMn_{0.95}V_{0.05}O₃, while its NO conversion was improved only at this temperature as compared to the parent LaMnO₃ (Fig. 4B). Activity was significantly modified by means of simple-oxide supporting. As a result, LaMnO₃/CeO₂ exhibited the best NO and NH₃ conversions among all the prepared catalysts as well as an ideal low-temperature N₂ yield (<200 °C). An enhanced high-temperature NO conversion was associated with the TiO₂ supporting, while the highest N₂ selectivity at T > 250 °C and the worst NH₃ conversion was obtained over this LaMnO₃/TiO₂ catalyst. Supplementary experiment for investigating the internal mass transfer through varying the particle sizes of LaMnO₃ catalyst has been conducted at 150 °C (not shown), demonstrating that the internal mass transfer in the range of 0.25–0.42 mm is eliminated.

Based on above activity data, a further investigation was conducted on those samples having the relatively satisfactory SCR performances, in order to reveal the reasons for deNO_x activity improvements. Consequently, the Ce- or Fe-substituted (LaMn_{0.95}Fe_{0.05}O₃, La_{0.9}Ce_{0.1}MnO₃) and the supported (LaMnO₃/TiO₂, LaMnO₃/CeO₂) samples were thereafter analyzed by H₂-TPR, XPS and TPD, contrasting with the pure LaMnO₃.

3.3.2. Redox properties as evaluated by H₂-TPR

H₂-TPR patterns show the influence of Ce or Fe substitution as well as CeO₂ or TiO₂ supporting on the related redox abilities (Fig. 5 and Table 3). It is seen that Ce or Fe substitution hardly changes the reduction profile of LaMnO₃ apart from a drop of the total H₂ consumption of La_{0.9}Ce_{0.1}MnO₃. For the supported samples, the total H₂ consumptions were significantly suppressed, while the intense peak at 360 °C achieved over LaMnO₃ disappeared entirely, corresponding to a decrease of the amount of active LaMnO₃ component after simple-oxide supporting. The initial temperature for reduction shifted largely from 200 °C to 270 °C after TiO₂ support, implying an intimate interaction between Mnⁿ⁺ and TiO₂ [41].

According to our previous study, the reduction of LaMnO₃ here can be assigned to two steps: Mn⁴⁺ to Mn²⁺ (below 600 °C) and Mn²⁺ to Mn⁰ (above 600 °C) [16]. Furthermore, the first reduction step is in fact composed by two successive processes, Mn⁴⁺ → Mn³⁺ → Mn²⁺ [16,42]. Furthermore, the deconvolution for the first TPR peaks are illustrated in Fig. 5 (as the dotted lines),

Table 3
Results of H₂-TPR experiments.

Samples	Total H ₂ consumption (mmol g ⁻¹) ^a	H ₂ consumption of peak 1 (Mn ⁴⁺ → Mn ³⁺) (mmol g ⁻¹) ^b	Mn ⁴⁺ percentage (%) ^c	H ₂ consumption of peak 2+3 (Mn ³⁺ → Mn ²⁺) (mmol g ⁻¹) ^b	Reduced Mn ³⁺ percentage (%) ^d
LaMnO ₃	3.64	0.59	28.41	1.64	79.45
La _{0.9} Ce _{0.1} MnO ₃	3.14	0.66	32.06	1.46	70.50
LaMn _{0.95} Fe _{0.05} O ₃ ^e	3.66	0.69	34.91	1.79	91.31
LaMnO ₃ /CeO ₂	1.41	—	—	—	—
LaMnO ₃ /TiO ₂	1.09	—	—	—	—

^a The total H₂ consumption amount for per gram material, issued from the H₂-TPR experiment and calculated by deconvolution of the reduction peaks.

^b The H₂ consumption of each peak.

^c The percentages of Mn⁴⁺ in Mnⁿ⁺ were calculated according to H₂ consumptions of Mn⁴⁺ to Mn³⁺ (peak 1).

^d The reduced percentages of Mn³⁺ to Mn²⁺ after Mn⁴⁺ was reduced to Mn³⁺, relating to peaks 2 and 3.

^e Ignore the reduction of Fe³⁺ according to its low content (5%) and very limited reducibility in the substituted perovskites [20].

and their H₂ consumptions are summarized in Table 3. Actually, Mn⁴⁺/Mn³⁺ ratio was reported to be a key factor of SCR performance of the Mn-containing samples: a higher ratio leads to both a better NO conversion (by improving NO oxidation) and a lower N₂ selectivity (by enhancing unselective NH₃ oxidation) [10,39,43]. Consequently, to quantify the amount of Mn⁴⁺ seems to be helpful to explain the discrepancy on SCR activities. Fortunately, in the case of Ce- or Fe-substituted samples, Ce⁴⁺ or Fe³⁺ incorporation did not disturb Mn⁴⁺ reduction at 320 °C, due to their apparently higher reduction temperatures [20,44] (the existence of abundant Ce⁴⁺ in La_{0.9}Ce_{0.1}MnO₃ was already proved by XPS, not shown); for the supported samples, the reduction of CeO₂ or TiO₂ is also excluded in Mn⁴⁺ reduction zone since they were reported to occur above 550 °C [44–46]. These make the quantification of Mn⁴⁺ possible, by integrating the corresponding peak of Mn⁴⁺ → Mn³⁺ reduction for all LaMn-based samples.

As for the substituted and the parent samples, the superimposed low-temperature peaks were separated into three ones, which individually located at around 320 (peak 1), 360 (peak 2), 450 °C (peak 3). The first peak (peak 1) can be safely assigned to the process of Mn⁴⁺ → Mn³⁺ reduction while the last two peaks (peak 2 and 3) are related to the reduction of Mn³⁺ to Mn²⁺. Furthermore, peak 2 could be regarded as the reduction of Mn³⁺ from surface and

subsurface, which is easier to participate in the reduction, comparing to those Mn³⁺ in the bulk (peak 3). According to the noticeable enhancements for H₂ consumption in peak 1 (Table 3), more Mn⁴⁺ generated in LaMn-based perovskite structure after Ce or Fe substitution, achieving better redox capacities. Additionally, it has been recently verified that more lattice oxygens in perovskite could be activated via substitution by highly reducible ions, presenting better oxygen migration ability [20]. After quantification of peak 1, Mn⁴⁺ accounts for 28.41% of the total amount of Mnⁿ⁺ in LaMnO₃ sample, confirming the structure of LaMnO_{3.15}, which has 30% of Mn⁴⁺. There is a slight increase of Mn⁴⁺ proportion in the case of Ce- or Fe-introduced samples, corresponding to 32.06% or 34.91% of Mn⁴⁺. Subsequently, 79.45%, 70.50% and 91.31% of Mn³⁺ were reduced to Mn²⁺ in the following two peaks, respectively for the parent, Ce- and Fe-substituted samples (Table 3).

It is a little different for TPR curves of the supported samples that only two moderate peaks were obtained after TiO₂ or CeO₂ dilution. The first peak obtained from LaMnO₃/CeO₂ still centered at 320 °C. However, TiO₂ supporting led to an obviously delay of this temperature to 410 °C, showing a remarkable decrease in redox capacity. Surprisingly, the calculated Mn⁴⁺ proportion is beyond 100% of Mnⁿ⁺ according to the first peak for either of these two samples, implying a combination of peak 1 for Mn⁴⁺ → Mn³⁺ reaction and peak 2 for Mn³⁺ → Mn²⁺ reduction (Fig. 5). Therefore, it becomes impossible to quantify the proportions of Mn⁴⁺ for these two materials. CeO₂ supporting apparently increased the redox capacity of surface and subsurface Mn³⁺ with respect to pure LaMnO₃ perhaps due to the decline of crystal sizes and the increase of surface areas (Table 1), while the opposite phenomenon appeared after TiO₂ supporting likely because of an intimate interaction between Mnⁿ⁺ and TiO₂.

Generally, cerium or iron substitution did not significantly alter the redox capacity of LaMnO₃, especially for the reduction temperature. Indeed, their reducibility was strongly dependent on the essential nature of the B-site Mnⁿ⁺ cations, because these substituting cations (Ce⁴⁺ or Fe³⁺) always have much lower redox capacities than Mnⁿ⁺ ones. It is similar to that taking place over LaMnO₃/CeO₂, while a strong interaction appeared between TiO₂ support and the loaded LaMnO₃ phase.

3.3.3. Surface element analysis evaluated by XPS

XPS analysis was also carried out to know the abundances and valences of the surface elements, with the results being listed in Fig. 6 and Table 4. LaMnO₃ exhibited the lowest surface La/Mn ratio with a value of 1.3, while this ratio was able to be improved slightly by Ce substitution. In contrast, Fe substitution even brought a 21% increment of Mn 2p peak (although the corresponding La/Mn ratio was slightly improved owing to a much higher increase of surface La content), showing an enhancement of surface Mnⁿ⁺ content. XPS data do not exactly allow quantifying the amounts of Mn⁴⁺,

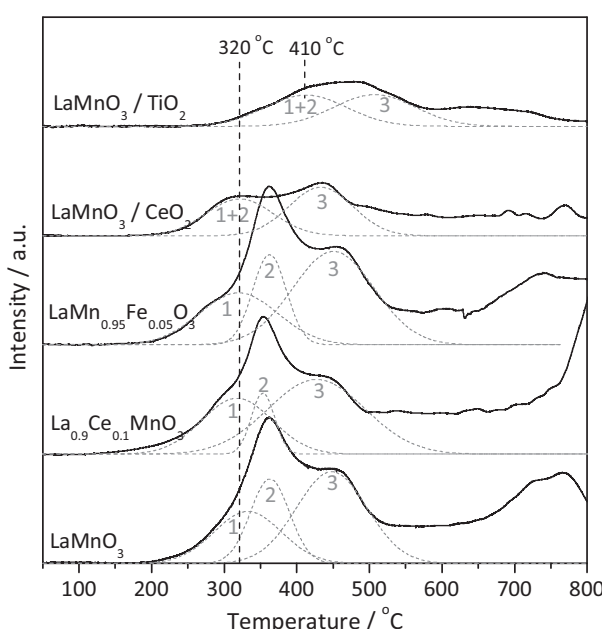


Fig. 5. H₂-TPR profiles obtained for LaMn-based samples. Peak 1: Mn⁴⁺ → Mn³⁺; peak 2: surface and subsurface Mn³⁺ → Mn²⁺; peak 3: bulk Mn³⁺ → Mn²⁺.

Table 4

XPS results for LaMn-based samples.

Samples	Surface abundance from XPS					
	La/Mn	O _{lattice} ^a	O _{adsorbed} ^a	O _{OH} ^{-a}	Total O ^a	Others (%)
LaMnO ₃	1.30	1.00	1.20	0.85	3.05	
La _{0.9} Ce _{0.1} MnO ₃	1.34	0.99	0.96	0.78	2.73	1.98 (Ce)
LaMn _{0.95} Fe _{0.05} O ₃	1.44	1.33	1.01	0.52	2.86	1.04 (Fe)
LaMnO ₃ /CeO ₂	1.80	1.16	0.86	0.30	2.32	8.84 (Ce)
LaMnO ₃ /TiO ₂	1.69	1.30	0.62	0.23	2.15	12.68 (Ti)

^a Relative surface abundance of each oxygen specie is calculated by deconvolution of the O 1s XPS peaks. The peak area of lattice oxygen over LaMnO₃ is denoted to be 1.00.

Mn³⁺ and Mn²⁺ on the surface, as mentioned in Section 3.2. No obviously shift can be observed after cationic substitutions, reflecting that the corresponding modifications in the surface Mn⁴⁺/Mn³⁺ ratio are quite limited. However, the peaks of Mn 2p for the both supported materials were largely reduced into about 22% of that for the pure LaMnO₃, owing to the dilution of surface Mnⁿ⁺ by support. Moreover, the supports also caused a slightly increase of the La/Mn ratio. The surface concentrations of Ce (8.84%) and Ti (12.68%) in LaMnO₃/CeO₂ and LaMnO₃/TiO₂ are much lower than their actual mol proportions (78% and 88%, calculated from the mass ratios of LaMnO₃: MO₂). This confirms a successful supporting, leading to a well coverage of MO₂ by LaMnO₃. Furthermore, the proportions of Mn⁴⁺ seemed to increase after MO₂ supporting since platforms between 640.9 and 642.5 eV are observed in the last two profiles.

The relative surface concentration of each oxygen species is also calculated through deconvolution of the O 1s XPS bands (see Table 4). The substitutions slightly decreased the total amount of surface oxygen species: all kinds of oxygen species, besides lattice oxygen, declined after the introduction of Ce⁴⁺. Fe³⁺ incorporation led to the higher value of lattice oxygen as well as the lower values of adsorbed and hydroxyl oxygen species. Both supports (CeO₂ and TiO₂) enhanced the lattice oxygen but seriously inhibited the other two oxygen species. These decreases can be safely related to the dilution of oxygen adsorption sites (Mnⁿ⁺ ions) over surface after supporting.

3.3.4. TPD of NO + O₂ or NH₃

During a heterogeneous catalytic reaction, the adsorption of reactants has been widely accepted to be an initial and crucial step, especially in a reaction following L-H mechanism. Additionally, this mechanism in NH₃-SCR of NO over LaMnO₃ perovskite has been proven by our previous study [47]. Consequently, the temperature programmed desorption was conducted after NO + O₂ or NH₃ adsorption at 200 °C, in order to evaluate the abilities of different catalysts for reactants adsorption. The results are presented in Fig. 7A and B and Table 5.

Fig. 7A shows NO, O₂ and N₂O signals during NO + O₂-TPD, while NO₂ and N₂ are undetectable below 500 °C. NO started to be desorbed at around 75 °C, accompanying with the considerable desorptions of O₂ and N₂O in the different temperature ranges (150–400 °C for N₂O, 300–500 °C for O₂). These results are very similar to those obtained over LaFe-based perovskites in our early study [15,18]. According to our experience, this desorption can be further divided into three stages: simple desorption of weakly chemisorbed NO (75–150 °C), NO desorption together with its dissociation (150–400 °C), and nitrite/nitrate thermal decomposition (300–500 °C). In the first stage, some weakly chemisorbed NO species can be desorbed at the relatively lower temperature. At the elevated temperatures, NO adspecies were activated, leading to a considerable NO desorption and a noticeable NO dissociation into N₂O. Above 300 °C, the surface nitrite/nitrate were decomposed parallel with an intense O₂ desorption.

In comparison with LaMnO₃, CeO₂ and TiO₂ supportings as well as Ce substitution showed the inferior abilities of total NO_x adsorptions, especially for the latter two samples, which is in contrast to LaMn_{0.95}Fe_{0.05}O₃. Besides, taking account that lattice oxygen could be rarely desorbed below 500 °C over LaMn-based perovskites [36], the O₂ desorbed here is mainly derived from the decomposition of nitrite/nitrate species. Therefore, the quantification of the corresponding NO desorptions occurring at the same temperature zone for O₂ desorption could determine the amounts of nitrites or nitrates over these tested samples, as listed in Table 5. In fact, the nitrite/nitrate amounts achieving over the substituted samples during TPD were roughly in line with the amounts of the surface adsorbed oxygen as determined by XPS (Table 4), rather than the total amounts of surface Mnⁿ⁺ cations. The important role of adsorbed oxygen species was detailedly discussed in Section 3.2. When redox capacities and surface areas are close, it is reasonable to correlate the oxygen adsorption capacity to nitrites/nitrates cumulant because these species generate at the oxygen adsorbed sites [15]. Compared with La_{0.9}Ce_{0.1}MnO₃, LaMnO₃/CeO₂ had a relatively lower coverage of surface adsorbed oxygen but obtained an even larger amount of nitrite/nitrate species, probably due to the high oxidizing ability of CeO₂ for NO to NO₂. Actually, it was reported that CeO₂ displayed a significant promotion on NO oxidation even at temperature as low as 100 °C, due to its excellent oxygen storage and redox properties [2]. Besides, it is not surprising that TiO₂ support did not lead to a remarkable nitrite/nitrate generation, because of its poorly redox properties caused by a strong

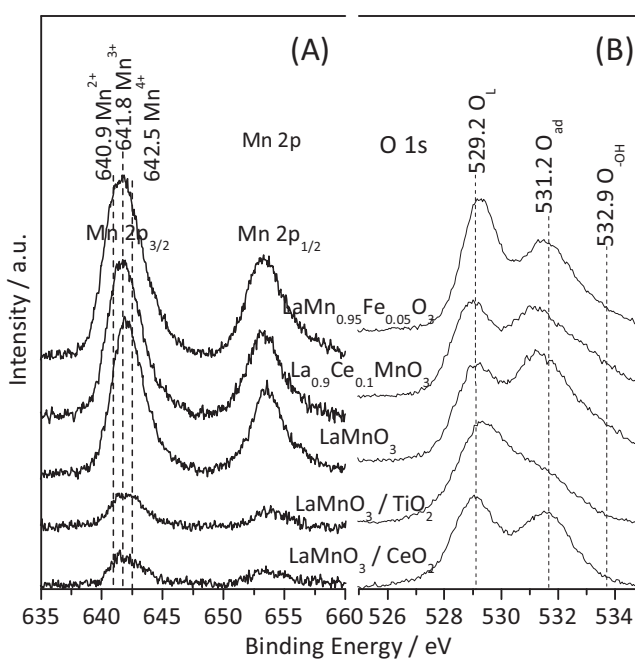


Fig. 6. XPS profiles for LaMn-based samples. (A) Mn 2p, (B) O 1s.

Table 5

Amounts of desorption species from LaMn-based materials during NO + O₂- and NH₃-TPD experiments.

Samples	Desorption amounts in NO + O ₂ -TPD ($\mu\text{mol g}^{-1}$)				Amount of NH ₃ in NH ₃ -TPD ($\mu\text{mol g}^{-1}$)
	NO ^a	Nitrite/Nitrate ^b	N ₂ O ^c	Total NO _x ^d	
LaMnO ₃	56.53	28.38	11.06	78.65	12.38
La _{0.9} Ce _{0.1} MnO ₃	36.01	17.46	5.69	47.39	9.74
LaMn _{0.95} Fe _{0.05} O ₃	58.33	24.07	22.86	104.05	15.46
LaMnO ₃ /CeO ₂	44.9	20.66	12.33	69.56	11.73
LaMnO ₃ /TiO ₂	25.01	2.90	13.53	52.07	29.89

^{a, c, e} The desorption amounts of NO or N₂O or NH₃ were calculated by quantification of the corresponding desorption evolutions.

^b The amounts of nitrites/nitrates were calculated by quantification of the corresponding NO desorption only occurring at the same temperature zone for O₂ desorption.

^d The amounts of total desorbed NO_x were derived from the sum of NO and N₂O (NO + 2 × N₂O).

Mnⁿ⁺-TiO₂ interaction, which limits the corresponding NO oxidation.

The evolutions of NH₃ desorption were recorded during NH₃-TPD, presenting in Fig. 7B and Table 5. Similar to NO desorption, the desorption curves of NH₃ allow to be divided into two parts as follows: the former part at lower temperature could be assigned to the desorption of NH₄⁺ weakly bound to surface hydroxyl group; and the latter one at higher temperature was attributed to the desorption of coordinated NH₃ bound to Lewis acid sites. It is unnecessary to further distinguish these two adNH₃ species, since both of them were previously reported to be active to participate in the SCR process through reaction with adNO_x species to form the important intermediates [10,48]. Surprisingly, LaMnO₃/TiO₂, which showed the weakest nitrite/nitrate desorption, exhibited herein extremely improvement on NH₃ desorption, with a much higher amount (29.89 $\mu\text{mol g}^{-1}$, Table 5) comparing to the other samples. More importantly, Ti ions were reported to be the excellent NH₃ adsorption sites, even better than Mnⁿ⁺ [10]. Furthermore, its largest surface area is also beneficial. Differently, another supported catalyst of LaMnO₃/CeO₂ showed a slightly decline for NH₃ adsorption as compared to LaMnO₃, even though with an improved surface area. Lowest amount of NH₃ desorption was obtained over the Ce-substituted sample, also displaying an inhibition effect of Ce for NH₃ adsorption, by either substitution or supporting. The introduction of Fe³⁺ brought an apparent enhancement, due to the enrichment of Mnⁿ⁺ on the surface.

3.3.5. DRIFTS studies of stepwise exposure to NO + O₂ and/or NH₃.

Being an effective method for reactants adsorption and surface reaction analysis, DRIFTS study was carried out at 200 °C for a further investigation over the representative sample – LaMnO₃. Fig. 8A shows the surface species adsorbed with an exposure to NO and O₂. Within the first 10 min, abundant of linear nitrite (at 1270 cm⁻¹) [49] and chelating bidentate nitrate (at 1300, 1517 and 1540 cm⁻¹) [50–53] were generated, while monodentate nitrite (at 1400 and 1465 cm⁻¹) [50,54] and weakly adsorbed NO₂ (at 1633 cm⁻¹) [55,56] also appeared on the surface. These surface species correspond well to the surmise in NO + O₂-TPD. After a longer exposure, ionic nitrate (1350 cm⁻¹) started to yield and accumulated rapidly upon Mnⁿ⁺ ions, becoming dominant among all the nitrite/nitrate species. The same specie was previously detected over LaFe-based perovskites above 300 °C, showing a negative effect on C₃H₆-SCR of NO through a rather stable occupancy of active sites [18]. Adsorption is saturated after 30 min, followed by switching to NH₃ reductant. Surprisingly, except the fading away of adsorbed NO₂ at 1633 cm⁻¹, no obvious change on surface species was detected, although LaMnO₃ already presented a considerable activity (70% for NO conversion and 60% for NH₃ conversion) at this temperature. This result confirmed that the two kinds of adsorbed species – nitrites/nitrates and adNH₃ – actually shared the same

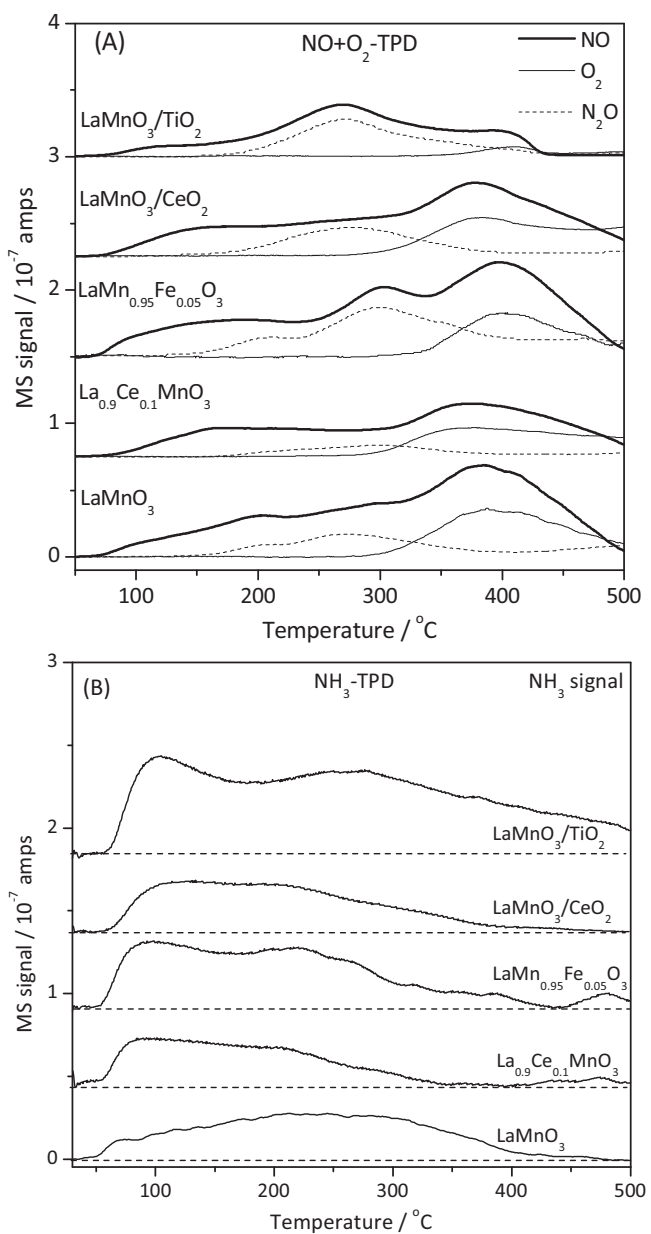


Fig. 7. NO + O₂- and NH₃-TPD profiles obtained for LaMn-based samples. (A) MS signals recorded for NO (thick line), O₂ (thin line) and N₂O (dotted line) during NO + O₂-TPD. (B) MS signals recorded for NH₃ during NH₃-TPD.

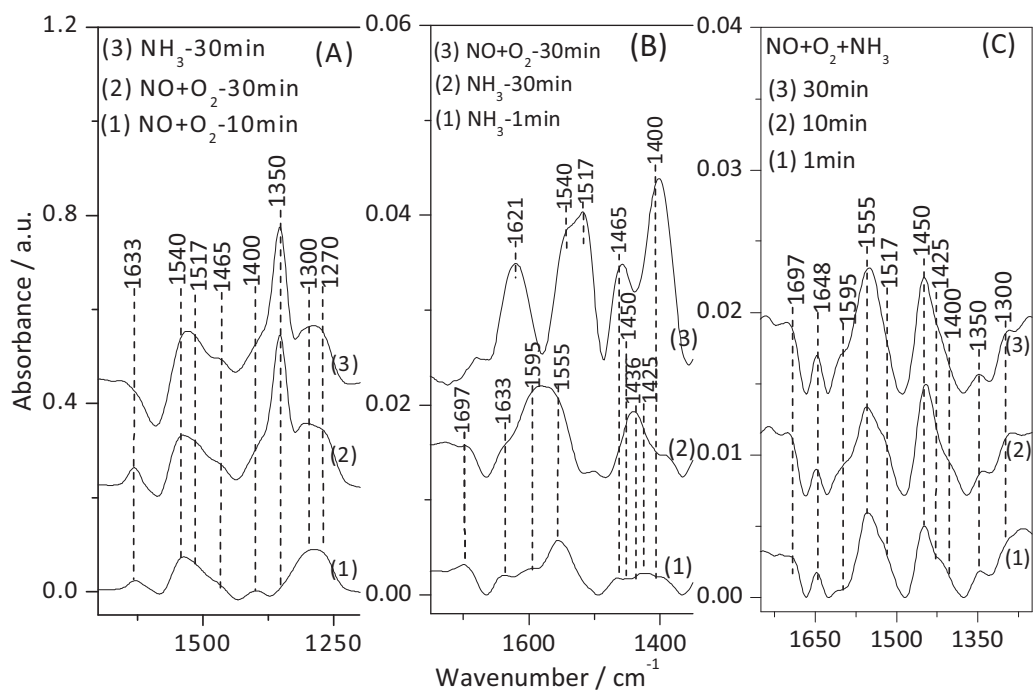


Fig. 8. In situ DRIFT spectra: (A) Exposure of LaMnO_3 to $\text{NO} + \text{O}_2$, followed by NH_3 . (B) Exposure of LaMnO_3 to NH_3 followed by $\text{NO} + \text{O}_2$. (A) Exposure of LaMnO_3 to $\text{NO} + \text{O}_2 + \text{NH}_3$. Conditions: $\text{NO} = 1000 \text{ ppm}$, $\text{NH}_3 = 1000 \text{ ppm}$, $\text{O}_2 = 6\%$, balanced by He. The adsorption temperature is 200°C .

adsorption sites of Mn^{n+} , and NO_x were adsorbed more firmly than NH_3 did.

A second DRIFTS experiment was designed to investigate the adsorption/activation of NH_3 in the absence of O_2 and to study the reactivity of the adsorbed NH_3 species toward NO . At the beginning of exposing the fresh LaMnO_3 to NH_3 , monodentate nitrate (at 1450 and 1555 cm^{-1}) [10,57] was formed quickly on the surface through oxidation of NH_3 by surface oxygen, accompanying with NH_3 chemisorption: NH_4^+ (at 1425 and 1436 cm^{-1}) and NH_3 (at 1595 and 1697 cm^{-1}) [50,58]. Small amount of NO_2 was also produced. The adsorption also reached a saturation after 30 min , only the adsorption of NH_3 (NH_4^+ and NH_3) enhanced strongly, due to the limitation of oxygen available for NH_3 oxidation under an O_2 absence atmosphere. This can be correlated to the abundant desorption of NH_3 in NH_3 -TPD. Switching to $\text{NO} + \text{O}_2$, the adNH_3 species vanished gradually, resulting in an intense accumulation of monodentate nitrite (at 1400 and 1465 cm^{-1}), chelating bidentate nitrate (at 1517 and 1540 cm^{-1}) and bridging nitrate (at 1621 cm^{-1}) [58,59]. This is different from the exposure of the NO_x adsorbed surface to NH_3 , indicating again that NH_3 adsorption is in a weaker strength as well as adNH_3 species has a higher reactivity than nitrite/nitrate species. In another word, nitrites/nitrates are more easily generated but harder to be activated at 200°C . Furthermore, the nitrite/nitrate amount declined sharply to only $1/20$ of those formed over the fresh surface (comparing Plot 3 of Fig. 8B with Plot 2 of Fig. 8A), implying an inhibition effect of adNH_3 species on the formation of $\text{NO}_2^-/\text{NO}_3^-$ species, which essentially contributes to suppress the possible NO oxidation on the surface under a less oxidizing or even reducing environment.

The co-adsorption results obviously supported the conclusions obtained in the former two DRIFTS investigations. The surface was mainly covered by monodentate nitrate and some other nitrite/nitrate species (at 1300 , 1350 , 1400 , 1450 , 1517 and 1555 cm^{-1}), while adNH_3 species remained to be much weaker (1425 , 1436 , 1595 and 1697 cm^{-1}). It is speculated that either an inhibition of nitrite/nitrate species (especially ionic nitrates appearing at 1350 cm^{-1}) or an enhancement of adNH_3 species could

be in favor of the further interaction between them, leading to the better NO and NH_3 conversions as well as N_2 yield.

It is worth noting, among all the nitrite/nitrate species which can generate on the surface, monodentate nitrate (at 1450 and 1555 cm^{-1}) was reported to be the real active adNO_x species for this SCR process [10,48]. The individual exposure to $\text{NO} + \text{O}_2$ did not allow to obtain this species (Plots 1–3 in Fig. 8A and Plot 3 in Fig. 8B), while this nitrate species became dominant in NH_3 adsorption and co-adsorption (Plots 1–2 in Fig. 8B and Plots 1–3 in Fig. 8C), illustrating that the intensely oxidizing environment was adverse to the formation of monodentate nitrate. Moreover, the ionic nitrate species were totally inhibited in the presence of NH_3 , reducing the occupation of Mn^{n+} by these inert species, which would be surely positive for SCR activity. As verified in our early study on C_3H_6 -SCR of NO over $\text{LaFe}_{0.8}\text{Cu}_{0.2}\text{O}_3$, the activity was strongly depressed, even if the reductant $\text{C}_x\text{H}_y\text{O}_z$ can be easily generated on its surface, due to the abundant surface accumulation of ionic nitrates [18]. Herein, we can conclude the crucial roles of NH_3 on this SCR process:

- (1) The reductant to react with nitrites/nitrates.
- (2) To depress the abundant accumulation of nitrites/nitrates on the surface.
- (3) Induce to the main formation of active monodentate nitrate while inhibiting the other nitrites/nitrates (especially for the inert ionic nitrates).

All of them can ensure the following reaction between monodentate nitrate and $\text{NH}_4^+/\text{NH}_3$. However, in fact, the participation of the other nitrite/nitrate species in this SCR reaction can not be fully excluded.

3.3.6. Correlations among TPR, XPS, TPD, DRIFTS and activity test

It is widely accepted that in a typical heterogeneous catalytic reaction, the adsorption of reactants and the activation of adsorbed species are both indispensable for the further process. In DRIFTS experiment, it has been confirmed that the nitrites/nitrates were relatively inactive and more strongly adsorbed over LaMnO_3

with respect to *adNH₃* species, even though their amounts were detected to be largely decreased in the presence of NH₃. From NO + O₂-TPD, we found that excess nitrites/nitrates cumulant was obviously depressed by cationic substitution to various degrees (cumulants: LaMnO₃ > LaMn_{0.95}Fe_{0.05}O₃ > La_{0.9}Ce_{0.1}MnO₃), which causes a reverse order of NO conversions [La_{0.9}Ce_{0.1}MnO₃ (87.3%)>LaMn_{0.95}Fe_{0.05}O₃ (78.5%)>LaMnO₃ (70.5%)] at 200 °C. This strongly implies that the depression of the surface nitrites/nitrates could be a key on SCR behaviors. Herein, the contribution of the difference abilities on NH₃ adsorption over the perovskite-type catalyst seems not to be decisive because La_{0.9}Ce_{0.1}MnO₃ associated with less NH₃ adsorption was still active under this condition during SCR process. In fact, another important factor of redox properties was believed to determine the activation on the interaction between relatively reactive nitrites/nitrates and *adNH₃*, while the smallest amount of active Mn⁴⁺ of LaMnO₃ along with a relatively poor redox properties as compared to the substituted samples may also limit its activity. In the case of LaMnO₃/TiO₂, the lowest nitrites/nitrates and the highest *adNH₃* cumulants led to a surprising decline for NO conversion below 250 °C, demonstrating the serious restriction by its weak redox ability, which limited the NO oxidation as well as the activation of chemisorbed species at low temperatures. Besides, the activity increased intensely over LaMnO₃/TiO₂ at T>250 °C, attributing to the maximum NH₃ adsorption. Similarly, the best NO conversion of 100% was achieved over LaMn_{0.95}Fe_{0.05}O₃ at 300 °C, also profiting from an improvement of NH₃ adsorption. Moreover, LaMnO₃/CeO₂ exhibited an expectably high activity below 200 °C, which can be safely correlated to the enhancement of NO oxidation by CeO₂ at low temperature zone, where Mnⁿ⁺ itself showed insufficient oxidation abilities [2]. In addition, both of the high dispersion of Mnⁿ⁺ and its high surface area may also be favorable. In the case of N₂ yield, the higher N₂ yields are commonly associated with the better NO conversions for all the modified samples, except that the best N₂ selectivity at T>250 °C is achieved over LaMnO₃/TiO₂ whose lowest redox capacity is surely in favor of this.

The results presently obtained do not allow us to directly correlate the different ratios of Mn⁴⁺/Mn³⁺ (surface or total) with their diverse NO conversions and N₂ yields. Nevertheless, we believe that this ratio represents essentially the redox capacity of a Mn-based catalyst. Generally, the higher this ratio is, the better its redox capacity is. However, for some reason, the redox capacity could decline without a decrease of Mn⁴⁺/Mn³⁺. As for LaMnO₃/TiO₂, it was detected to have enhanced Mn⁴⁺/Mn³⁺ ratio on the surface (XPS) but the lowest redox capacity, leading to a lower NO conversion and higher N₂ selectivity at low-temperature zone. Nevertheless, it is still not suitable to simply correlate the redox capacity to the activity of SCR of NO by NH₃, especially at higher temperatures. In brief, at low-temperature zone where NO oxidation is limited, a better redox capacity indeed facilitates to achieve a considerable activity. At high-temperature zone where catalyst exhibits sufficient NO oxidation ability, a better activity depends on more *adNH₃* and less nitrite/nitrate accumulations. Additionally, a lower redox capacity could lead a higher N₂ selectivity through inhibiting unselective oxidation of NO and NH₃.

4. Conclusions

In this study, a beneficial effect of LaMnO₃ perovskite structure was verified by comparing to the corresponding amorphous precursor and the simple-oxide mixture for NH₃-SCR of NO, due to the great enrichments of active sites of Mnⁿ⁺ ions as well as active oxygen species on the surface when the perovskite structure is well formed.

The partial substitutions of La or Mn by different metal cations (Ce, Sr, Fe, V) as well as the supporting by CeO₂ or TiO₂ could significantly change the SCR activity of LaMnO₃, through modifying the redox capacity as well as changing the nitrites/nitrates cumulant. Among the nitrite/nitrate species formed over LaMnO₃, monodentate nitrates are identified to be reactive with *adNH₃*, while ionic nitrates are totally inert. The enhancement in NO oxidation apparently contributed to a better low-temperature (<200 °C) activity over LaMnO₃/CeO₂, while the depression to an abundant accumulation of nitrites/nitrates (especially for the inert ionic nitrates) was deemed to be crucial for higher activity at high-temperature region (≥200 °C), where NO oxidation is sufficient. In addition, a higher NH₃ adsorption ability and higher dispersion of Mnⁿ⁺ can be also favorable for an ideal SCR performance.

Acknowledgements

Runduo Zhang sincerely acknowledges the National Natural Science Foundation of China under Grant (Nos. 20977004, 21177008 and 21121064), National 863 Program (2013AA065900) and the New Century Program for Excellent Talents in University (NCET-10-0204) for the financial support. Wei Yang also thanks to the China Scholarship Council (CSC) for its financial support through a one-year abroad Ph.D. stay.

References

- [1] H. Bosch, F. Janssen, *Catalysis Today* 2 (1988) 369–521.
- [2] G. Qi, R.T. Yang, *Journal of Catalysis* 217 (2003) 434–441.
- [3] C.N. Costa, V.N. Stathopoulos, V.C. Belessi, A.M. Efstatthiou, *Journal of Catalysis* 197 (2001) 350–364.
- [4] C.N. Costa, P.G. Savva, C. Andronikou, P.S. Lambrou, K. Polychronopoulou, V.C. Belessi, V.N. Stathopoulos, P.J. Pomonis, A.M. Efstatthiou, *Journal of Catalysis* 209 (2002) 456–471.
- [5] C.N. Costa, A.M. Efstatthiou, *Applied Catalysis B* 72 (2007) 240–252.
- [6] C.N. Costa, P.G. Savva, J.L.G. Fierro, A.M. Efstatthiou, *Applied Catalysis B* 75 (2007) 147–156.
- [7] P.G. Savva, A.M. Efstatthiou, *Journal of Catalysis* 257 (2008) 324–333.
- [8] G.G. Olympiou, A.M. Efstatthiou, *Chemical Engineering Journal* 170 (2011) 424–432.
- [9] Z. Liu, J. Li, S.I. Woo, *Energy and Environmental Science* 5 (2012) 8799–8814.
- [10] F. Liu, H. He, Y. Ding, C. Zhang, *Applied Catalysis B* 93 (2009) 194–204.
- [11] J. Li, J. Chen, R. Ke, C. Luo, J. Hao, *Catalysis Communications* 8 (2007) 1896–1900.
- [12] Z. Wu, R. Jin, Y. Liu, H. Wang, *Catalysis Communications* 9 (2008) 2217–2220.
- [13] L. Singoredjo, R. Korver, F. Kapteijn, J. Moulijn, *Applied Catalysis B* 1 (1992) 297–316.
- [14] Z. Zhu, Z. Liu, H. Niu, S. Liu, *Journal of Catalysis* 187 (1999) 245–248.
- [15] R. Zhang, A. Villanueva, H. Alamdari, S. Kaliaguine, *Journal of Catalysis* 237 (2006) 368–380.
- [16] R. Zhang, A. Villanueva, H. Alamdari, S. Kaliaguine, *Applied Catalysis A* 307 (2006) 85–97.
- [17] R. Zhang, A. Villanueva, H. Alamdari, S. Kaliaguine, *Applied Catalysis B* 64 (2006) 220–233.
- [18] W. Yang, R. Zhang, B. Chen, D. Duprez, S. Royer, *Environmental Science and Technology* 46 (2012) 11280–11288.
- [19] R. Zhang, H. Alamdari, S. Kaliaguine, *Journal of Catalysis* 242 (2006) 241–253.
- [20] W. Yang, R. Zhang, B. Chen, N. Bion, D. Duprez, S. Royer, *Journal of Catalysis* 295 (2012) 45–58.
- [21] S. Royer, H. Alamdari, D. Duprez, S. Kaliaguine, *Applied Catalysis B* 58 (2005) 273–288.
- [22] M. Alfanti, M. Florea, V.I. Parvulescu, *Applied Catalysis B* 70 (2007) 400–405.
- [23] V. Szabo, M. Bassir, A. Van Neste, S. Kaliaguine, *Applied Catalysis B* 37 (2002) 175–180.
- [24] P. Porta, S. De Rossi, M. Faticanti, G. Minelli, I. Pettiti, L. Lisi, M. Turco, *Journal of Solid State Chemistry* 146 (1999) 291–304.
- [25] K. Stephan, M. Hackenberger, D. Kießling, G. Wendt, *Catalysis Today* 54 (1999) 23–30.
- [26] O. Kröcher, M. Elsener, *Applied Catalysis B* 92 (2009) 75–89.
- [27] L.A. Isupova, A.A. Budneva, E.A. Paukshtis, V.A. Sadykov, *Journal of Molecular Catalysis A* 158 (2000) 275–280.
- [28] P. Courty, H. Ajot, C. Marcilly, B. Delmon, *Powder Technology* 7 (1973) 21–38.
- [29] B. Shen, T. Liu, N. Zhao, X. Yang, L. Deng, *Journal of Environmental Sciences-China* 22 (9) (2010) 1447–1454.
- [30] J.B.A.A. Elemans, B. Van Laar, K.R. Van Der Veen, B.O. Loopstra, *Journal of Solid State Chemistry* 3 (1971) 238–242.
- [31] M. Crespin, W.K. Hall, *Journal of Catalysis* 69 (2) (1981) 359–370.

[32] P. Ciambelli, S. Cimino, G. Lasorella, L. Lisi, S. De Rossi, M. Faticanti, G. Minelli, P. Porta, *Applied Catalysis B* 37 (2002) 231–241.

[33] V.N. Stathopoulos, C.N. Costa, P.J. Pomonis, A.M. Efstratiou, *Topics in Catalysis* 16/17 (2001) 231–235.

[34] G. Sinquin, J.P. Hindermann, C. Petit, A. Kiennemann, *Catalysis Today* 54 (1999) 107–118.

[35] M. Kantcheva, M.U. Kucukkal, S. Suzer, *Journal of Molecular Structure* 482–483 (1999) 19–22.

[36] C.-L. Li, Y.-C. Lin, *Applied Catalysis B* 107 (2011) 284–293.

[37] K. Tabata, Y. Hirano, E. Suzuki, *Applied Catalysis A* 170 (1998) 245–254.

[38] M. Ghaffari, M. Shannon, H. Hui, O.K. Tan, A. Irannejad, *Surface Science* 606 (2012) 670–677.

[39] M. Kang, E.D. Park, J.M. Kim, J.E. Yie, *Applied Catalysis A* 327 (2007) 261–269.

[40] A.M. Efstratiou, K. Fliatoura, *Applied Catalysis B* 6 (1995) 35–59.

[41] Y. Okamoto, H. Gotoh, K. Hishida, H. Aritani, T. Tanaka, S. Yoshida, *Applied Surface Science* 121–122 (1997) 509–512.

[42] B. Levasseur, S. Kaliaguine, *Applied Catalysis A* 343 (2008) 29–38.

[43] F. Kapteijn, L. Singoredjo, A. Andreini, J.A. Moulijn, *Applied Catalysis B* 3 (1994) 173–189.

[44] Y. Sun, S.S. Hla, G.J. Duffy, A.J. Cousins, D. French, L.D. Morpeth, J.H. Edwards, D.G. Roberts, *International Journal of Hydrogen Energy* 36 (2011) 79–86.

[45] S.M. de Lima, A.M. da Silva, L.O.O. da Costa, J.M. Assaf, L.V. Mattos, R. Sarkari, A. Venugopal, F.B. Noronha, *Applied Catalysis B* 121–122 (2012) 1–9.

[46] H. Zhu, Z. Qin, W. Shan, W. Shen, J. Wang, *Journal of Catalysis* 225 (2004) 267–277.

[47] R. Zhang, N. Luo, W. Yang, N. Liu, B. Chen, *Journal of Molecular Catalysis A* 371 (2013) 86–93.

[48] R.Q. Long, R.T. Yang, *Journal of Catalysis* 190 (2000) 22–31.

[49] Y. Chi, S.S.C. Chuang, *Journal of Catalysis* 190 (2000) 75–91.

[50] G. Qi, R.T. Yang, *Journal of Physical Chemistry B* 108 (2004) 15738–15745.

[51] M. Kantcheva, *Journal of Catalysis* 204 (2001) 479–494.

[52] Y. Yu, H. He, Q. Feng, H. Gao, X. Yang, *Applied Catalysis B* 49 (2004) 159–171.

[53] S.D. Stasio, V.D. Santo, *Applied Surface Science* 253 (2006) 2899–2910.

[54] S. Kameoka, Y. Ukitu, T. Miyadera, *Physical Chemistry Chemical Physics* 2 (2000) 367–372.

[55] G. Qi, R.T. Yang, R. Chang, *Applied Catalysis B* 51 (2004) 93–106.

[56] K. Hadjivanov, H. Knözinger, *Physical Chemistry Chemical Physics* 2 (2000) 2803–2806.

[57] H. He, C. Zhang, Y. Yu, *Catalysis Today* 90 (2004) 191–197.

[58] D.A. Peña, B.S. Uphade, E.P. Reddy, P.G. Smirniotis, *Journal of Physical Chemistry B* 108 (2004) 9927–9936.

[59] F. Liu, H. He, C. Zhang, W. Shan, X. Shi, *Catalysis Today* 175 (2011) 18–25.